# Supplemental Materials for "Soil respiration phenology improves modeled phase of terrestrial net ecosystem exchange in northern hemisphere"

K. Arthur Endsley[1], John S. Kimball[1], and Rolf H. Reichle[2]

[1]Numerical Terradynamic Simulation Group (NTSG), W.A. Franke College of Forestry and Conservation, University of Montana, Missoula, MT
[2]Global Modeling and Assimilation Office, NASA Goddard Space Flight Center, Greenbelt, Maryland, USA

## Appendix A: Soil Hydrology Model

The soil hydrology model developed for this study proceeds in four main steps that are repeated for each daily time step. First, the maximum soil water infiltration rate, based on soil ice content and the land surface saturation fraction, is calculated. Second, soil water loss through potential transpiration is calculated based on the Priestly-Taylor method [Mu et al., 2011] and this is converted to actual transpiration in each soil layer based on the root distributions of Jackson et al. [1996] and soil water stress, based on the wilting point and field capacity estimates of Balland et al. [2008]. Third, the change in soil water content, $\Delta\,\theta$, is calculated based on Darcy's Law and the Richards equation. Finally, lateral drainage due to sub-surface saturation is removed and the soil water content in each layer is rebalanced so as to maintain physical limits.

The model uses daily average estimates of surface infiltration and potential transpiration rates to estimate daily changes in volumetric soil moisture, $\theta$, using sub-daily (e.g., hourly) time steps. Hydraulic conductivity, soil matric potential, and soil water diffusion (based on the Richards equation) are calculated as in CLM 5.0 [Lawrence et al., 2018], based on empirical equations from Clapp and Hornberger [1978] and Cosby et al. [1984]. Saturated hydraulic conductivity and saturated matric potential, both functions of soil texture, are calculated as in CLM 4.0. Soil texture, porosity, and daily surface infiltration (mm $s^{-1}$) are taken from the Catchment land model and SMAP L4SM. The fraction of the land surface that is saturated was calculated based on relative humidity [Mu et al., 2011], which was calculated from VPD and the saturation vapor pressure [Allen et al., 1998, Chapter 3]. Topographic slope was computed at each site based on the L4SM global 9-km elevation model.

The maximum surface infiltration rate is calculated as in CLM 5.0:

$$q_{max} = (1 - f_{sat})\Theta_{ice} k_{sat} \tag{1}$$

Where $f_{sat}$ is the fraction of the land surface that is saturated, $\Theta_{ice}$ is the impedance due to soil ice content, and $k_{sat}$ is the saturated hydraulic conductivity. The actual surface infiltration rate is taken to be the minimum of $q_{max}$ and the daily average rate from L4SM. The impedance due to ice is also calculated as in CLM 5.0:

$$\Theta_{ice} = 10^{-\Omega F_{ice}} \quad \text{where} \quad F_{ice} = \theta \frac{f_{ice}}{\theta_{sat}} = \frac{\theta_{ice}}{\theta_{sat}}; \; \Omega = 6 \tag{2}$$

Where $f_{ice}$ is the ice fraction of the combined liquid and ice water volumes, after the empirical formulation by Decker and Zeng [2006, Equation 4]. For simplicity, explicit phase changes and ice content are not tracked; instead, $f_{ice}$ is used as an instantaneous estimate of ice content as a fraction of total soilmoisture.

Daily potential transpiration is calculated using the Priestly-Taylor method [Mu et al., 2011] and is reduced by a factor, $\beta$, representing plant water stress:

$$\beta = \left( \frac{\theta_{liq} - \theta_{WP}}{\theta_{FC} - \theta_{WP}} \right)^q \tag{3}$$

Where $\theta_{liq}$ is the liquid soil volumetric water content; $\theta_{FC}$ and $\theta_{WP}$ are the soil moisture at field capacity and at wilting point, respectively; and $q$ is an empirical coefficient describing the curvature of the relationship between transpiration and available soil water [Verhoef and Egea, 2014]. We set $q = 1$ for this study. Field capacity and wilting point were defined based on soil texture using the empirical relationships of Balland et al. [2008]. Actual transpiration (potential transpiration reduced by $\beta$) is partitioned across the soil layers using the empirical root profiles of Jackson et al. [1996, Table 1], based on matching PFTs; the Evergreen Needleleaf PFT is the average of the boreal forest and temperate coniferous types of Jackson et al. [1996].

The surface infiltration rate and the transpiration from each layer represent two key source and sink terms, respectively, in the water balance equation, which is identical to that used in CLM 5.0 [Lawrence et al., 2018]:

$$\Delta z_i \frac{\partial \theta_{liq,i}}{\partial t} = -q_{i-1} + q_i - e_i$$

Where $\Delta z_i$ is the thickness (mm) of soil layer $i$, $q_{i-1}$ is the flow into layer $i$ from above (layers are enumerated downward from the surface), $q_i$ is the flow out of layer $i$ to the layer below, and $e_i$ is the hydraulic sink of transpiration loss. For the surface layer, $q_{i-1}$ is equal to the surface infiltration rate. Equation , applied to each soil layer, forms a sparse, tridiagonal system of equations where the change in liquid soil moisture in each layer, $\Delta\theta_{liq}$, is solved for simultaneously.

There are two additional, potential hydraulic sinks that are computed separately: free drainage from the bottom layer and lateral drainage in the presence of sub-surface saturation, including from perched, saturated zones. The free drainage condition is equivalent to the "flux" boundary condition of CLM 5.0 [UCAR, 2020] and is based on the hydraulic conductivity, $k$, and derivative of $k$ of the bottom layer:

$$q_{drain} = k_i + \left[ \frac{\partial\, k}{\partial\, \theta_{liq}} \times \Delta\theta_{liq} \right]_i \tag{4}$$

When the soil column is saturated from the bottom-up, lateral drainage from the saturated layer(s) is calculated after CLM 4.5 [Oleson et al., 2013]:

$$q_{drain} = \Theta_{ice}\, 10 \sin(\gamma) \exp(-f_{drain} z_{\nabla}) \quad \text{where} \quad f_{drain} = 2.5\,\mathrm{m}^{-1} \tag{5}$$

Where $\gamma$ is the topographic slope and $z_{\nabla}$ is the depth to the water table (top of saturated zone). Lateral drainage from a perched, saturated zone is also calculated after CLM 4.5:

$$q_{perch} = 10^{-5} \sin(\gamma) \left( \frac{\sum_{i=j}^{i=k} \Theta_{ice,i}\, k_{sat}(z_i)\, \Delta z_i}{\sum_{i=j}^{i=k} \Delta z_i} \right) (z_{frost} - z_{\nabla,perch}) \tag{6}$$

Where $j$ and $k$ are the soil layers that are perched and frozen (first such layer counting down from the surface), respectively, and $z_{frost}$ and $z_{\nabla,perch}$ are the depths to the frozen and perched layers.

After the change in liquid soil moisture is applied and lateral drainage is removed, soil moisture is manually re-balanced so as to maintain each layer within physical limits of $1\,\mathrm{mm} \leq \theta_{liq,i} \Delta z_i \leq (\phi - \theta_{ice,i}) \Delta z_i$, as described in Lawrence et al. [2018]. While the maximum surface infiltration rate and the actual transpiration rate are calculated once per day, the remaining steps are taken using sub-daily time intervals, usually less than 1 hour, and the soil moisture of the time final step is recorded as a daily snapshot and used as the initial conditions for the next day. The sub-daily time step varies according to the adaptive time-stepping scheme of CLM 5.0 [Lawrence et al., 2019]. All modeled sites are spun-up over a 20-year period to equilibrium soil moisture using a 365-day climatology of driver datasets.

# Supplemental Tables

Table S1: The 25 COSORE datasets used in this study. *These sites provided concurrent, daily soil moisture and temperature measurements along with CO2 flux. **This site was reported as "Open shrubland" and was mapped to the MOD12Q1 PFT "Shrubland." ***This "wetland" site is a northern peatland and was mapped to MOD12Q1 PFT "Grassland."

| Dataset | PFT | Citation |
|---|---|---|
| d20190424_ZHANG_maple | DBF | [Zhang et al., 2018] |
| d20190424_ZHANG_oak | DBF | [Zhang et al., 2018] |
| d20200212_ATAKA* | DBF | [Ataka et al., 2014] |
| d20200212_KAYE_LNE* | DBF | n.a. |
| d20200212_KAYE_LNW* | DBF | n.a. |
| d20200212_KAYE_LSE* | DBF | n.a. |
| d20200212_KAYE_LSW* | DBF | n.a. |
| d20200212_KAYE_UNE* | DBF | n.a. |
| d20200212_KAYE_USE* | DBF | n.a. |
| d20200212_KAYE_USW* | DBF | n.a. |
| d20200221_MATHES | DBF | [Curtis et al., 2005] |
| d20200224_MATHES | DBF | [Detto et al., 2013] |
| d20200328_UEYAMA_TESHIO | DNF | [Ueyama et al., 2018] |
| d20200228_RENCHON | EBF | n.a. |
| d20200108_JASSAL | ENF | [Jassal et al., 2008] |
| d20200114_CARBONE_SC_EMBUDO* | ENF | [Carbone et al., 2011] |
| d20200114_CARBONE_SC_SAUCE* | ENF | [Carbone et al., 2013] |
| d20200120_CHANG* | ENF | [Chang et al., 2008] |
| d20200122_BLACK | ENF | [Gaumont-Guay et al., 2014] |
| d20200220_GAVAZZI | ENF | [Noormets et al., 2010] |
| d20200417_ARAIN_TP39 | ENF | [Arain, 2018] |
| d20200331_PEICHL | GRS*** | [Järveoja et al., 2018] |
| d20200423_OYONARTE* | GRS | [Vargas et al., 2018] |
| d20191017_BALDOCCHI | SHB | [Baldocchi et al., 2006] |
| d20200423_SANCHEZ-CANETE* | SHB** | [Sánchez-Cañete et al., 2016] |

Table S2: Day-of-year (DOY) of NEE minimum, RECO maximum for EC flux towers ("Towers") and mean difference in DOY (experiment minus Towers), in days, for each experiment, based on the mean NEE seasonal cycle, identified using a low-pass filter, for all sites above 40 degrees N latitude.

| Product | Peak RECO DOY | Peak NEE DOY | RECO Phase (days) | NEE Phase (days) |
|---|---|---|---|---|
| Towers | 197 | 181 | n.a. | n.a. |
| NRv8.3 | 183 | 196 | -14 | +15 |
| NRv8.3 + Kok Effect | 184 | 196 | -13 | +15 |
| NRv8.3 + Litterfall Phenology | 187 | 182 | -10 | +1 |
| NRv8.3 + O2 Limit | 186 | 186 | -11 | +5 |
| NRv8.3 + Soil Profile | 185 | 186 | -12 | +5 |
| NRv8.3 + O2 Limit + Litterfall | 187 | 182 | -10 | +1 |
| NRv8.3 + Soil Profile + Litterfall | 186 | 183 | -11 | +2 |
| NRv8.3 + Soil Profile + O2 Limit | 186 | 186 | -11 | +5 |
| NRv8.3 + Soil Profile + O2 Limit + Litterfall | 186 | 183 | -11 | +2 |

Table S3: Mean difference in day-of-year (DOY) of NEE minimum, RECO maximum for each experiment compared to that of EC flux towers (experiment minus Towers), based on the seasonal cycle north of 40 degrees N latitude using Fourier regression. Standard deviation across PFTs is shown in parentheses.

| Product | RECO Phase (days) | NEE Phase (days) |
|---|---|---|
| Towers | n.a. ( 4.7) | n.a. (14.6) |
| NRv8.3 | -12.0 ( 4.7) | 26.2 (17.6) |
| NRv8.3 + Kok Effect | -11.9 ( 5.1) | 22.8 (15.4) |
| NRv8.3 + O2 Limit | -7.4 ( 4.5) | 11.0 (13.4) |
| NRv8.3 + Litterfall Phenology | -1.6 ( 7.3) | -4.7 ( 9.3) |
| NRv8.3 + Soil Profile | -9.4 ( 3.4) | 15.6 (13.1) |
| NRv8.3 + O2 Limit + Litterfall | -0.6 ( 6.2) | -17.9 (21.1) |
| NRv8.3 + Soil Profile + O2 Limit | -4.4 ( 5.5) | -7.2 (21.1) |
| NRv8.3 + Soil Profile + Litterfall | -4.8 ( 4.6) | 4.2 ( 9.6) |
| NRv8.3 + Soil Profile + O2 Limit + Litterfall | -2.3 ( 6.2) | -13.5 (18.4) |

Table S4: Day-of-year (DOY) of RECO maximum for EC flux towers ("Towers") and difference in DOY (experiment minus Towers), in days, for each experiment, based on the mean RECO seasonal cycle, identified using Fourier regression, for all sites above 40 degrees N latitude.

| Product | ENF | DNF | DBF | SHB | GRS | CCR | BCR |
|---|---|---|---|---|---|---|---|
| NRv8.3 | -11.9 | -20.2 | -10.9 | -6.2 | -4.8 | -10.5 | -19.6 |
| NRv8.3 + Kok Effect | -11.5 | -20.8 | -10.7 | -6.0 | -4.0 | -11.0 | -19.3 |
| NRv8.3 + O2 Limit | -8.8 | -18.8 | -5.0 | -3.1 | -2.4 | -4.4 | -9.0 |
| NRv8.3 + Litterfall Phenology | -8.0 | -11.3 | 2.7 | -1.6 | 0.9 | -1.4 | 7.7 |
| NRv8.3 + Soil Profile | -10.3 | -18.2 | -6.1 | -7.2 | -3.7 | -6.6 | -14.0 |
| NRv8.3 + O2 Limit + Litterfall | -5.9 | -10.3 | 2.1 | 1.0 | 1.1 | 1.5 | 6.1 |
| NRv8.3 + Soil Profile + O2 Limit | -8.4 | -15.5 | -1.4 | -4.7 | -2.9 | 0.7 | 1.3 |
| NRv8.3 + Soil Profile + Litterfall | -9.0 | -12.3 | -0.9 | -5.7 | -1.9 | -2.4 | -1.0 |
| NRv8.3 + Soil Profile + O2 Limit + Litterfall | -7.4 | -12.6 | 1.0 | -3.7 | -1.2 | 2.2 | 5.6 |

Table S5: Difference in day-of-year (DOY) of NEE minimum and RECO maximum for each experiment and for the EC flux towers ("Towers") compared to that of FLUXCOM (experiment/ Towers minus FLUXCOM), based on the seasonal cycle north of 40 degrees N latitude using Fourier regression.

| Product | RECO Phase (days) | NEE Phase (days) |
|---|---|---|
| Towers | +5.7 | -2.2 |
| NRv8.3 | -5.9 | +16.1 |
| NRv8.3 + Kok Effect | -5.8 | +16.2 |
| NRv8.3 + Litterfall Phenology | +3.4 | -8.2 |
| NRv8.3 + O2 Limit | -0.9 | +1.3 |
| NRv8.3 + Soil Profile | -2.7 | +6.5 |
| NRv8.3 + O2 Limit + Litterfall | +4.7 | -20.5 |
| NRv8.3 + Soil Profile + Litterfall | +1.0 | -3.3 |
| NRv8.3 + Soil Profile + O2 Limit | +2.1 | -24.6 |
| NRv8.3 + Soil Profile + O2 Limit + Litterfall | +3.9 | -28.2 |

Table S6: The mean $R_H$:$R_S$ ratios, and standard deviation in ratio across studies, from the Soil Respiration Database (SRDB) version 5, based on inferring Plant Functional Types from reported biome, ecosystem type, and leaf habit.

| PFT | Rh:Rs Ratio | Std. Dev. |
|---|---|---|
| DBF | 0.581 | 0.192 |
| EBF | 0.597 | 0.172 |
| ENF | 0.599 | 0.198 |
| GRS | 0.584 | 0.192 |
| SHB | 0.637 | 0.230 |
| Cropland | 0.642 | 0.210 |
| Other | 0.634 | 0.198 |

# Supplemental Figures

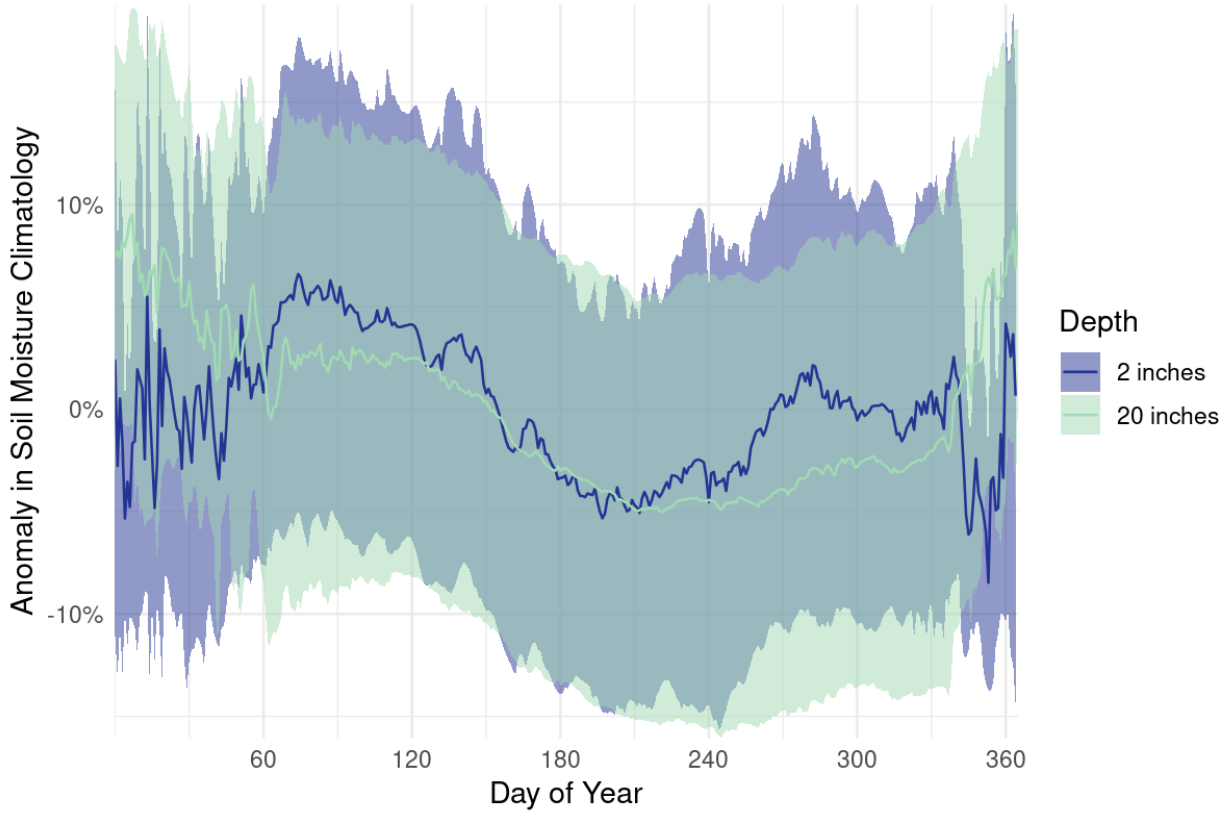


Figure S1: The mean seasonal cycle of soil moisture (SM) across USCRN and SCAN sites at the same depth north of 40 degrees N latitude. Very high variability is seen in the winter months, when *in situ* soil moisture measurement is less reliable, but a clear increase in surface soil moisture can be seen in spring. SM data were first cleaned, removing spikes and measurements during freezing conditions. SM measurements are unreliable at near or below freezing, which is the cause of the high variability seen in winter months.

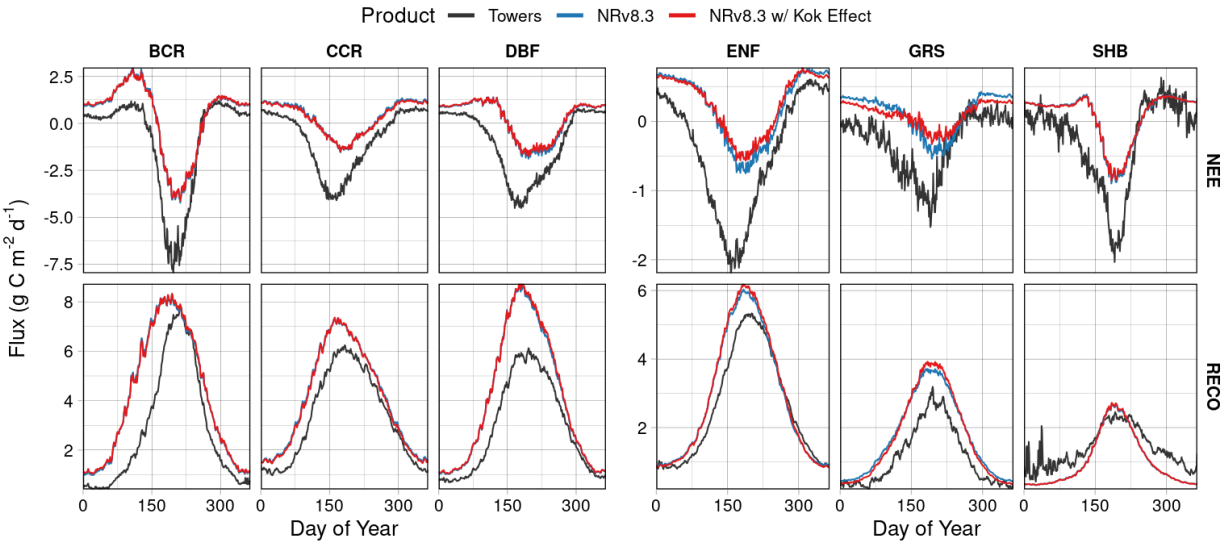


Figure S2: NEE and RECO seasonal cycles at each EC flux tower site in each PFT group, as modeled in the NRv8.3 + Kok Effect experiment.

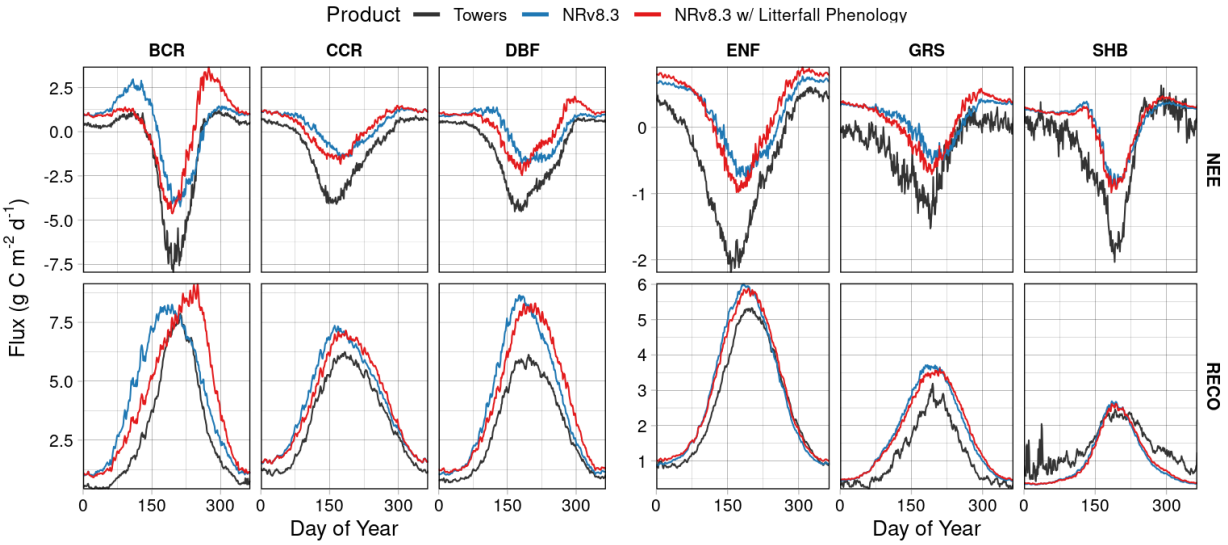


Figure S3: NEE and RECO seasonal cycles at each EC flux tower site in each PFT group, as modeled in the NRv8.3 + Litterfall Phenology experiment.

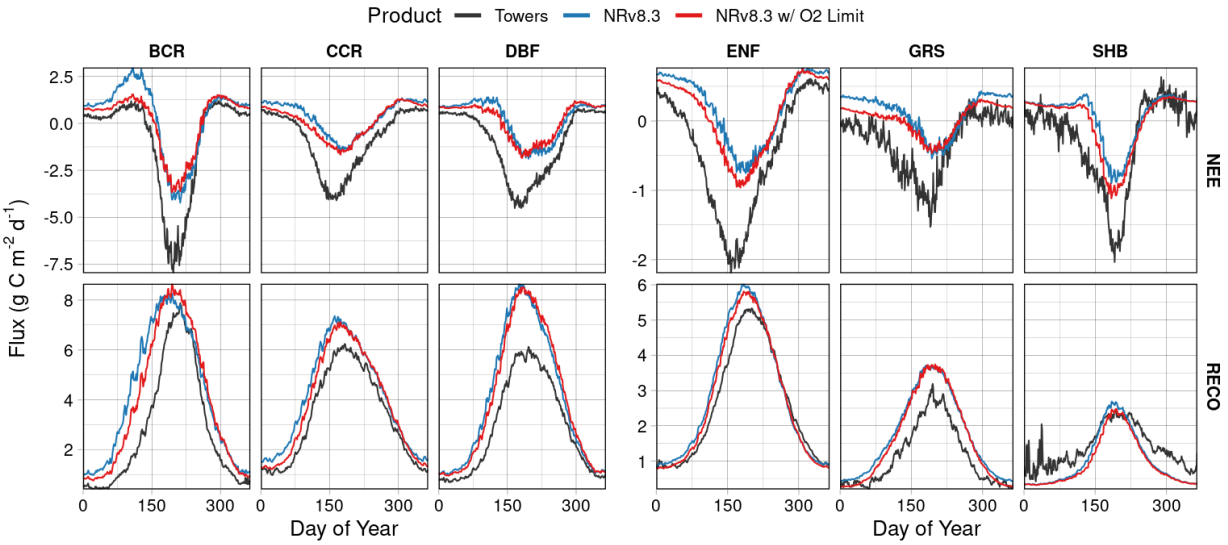


Figure S4: NEE and RECO seasonal cycles at each EC flux tower site in each PFT group, as modeled in the NRv8.3 + O2 Limit experiment.

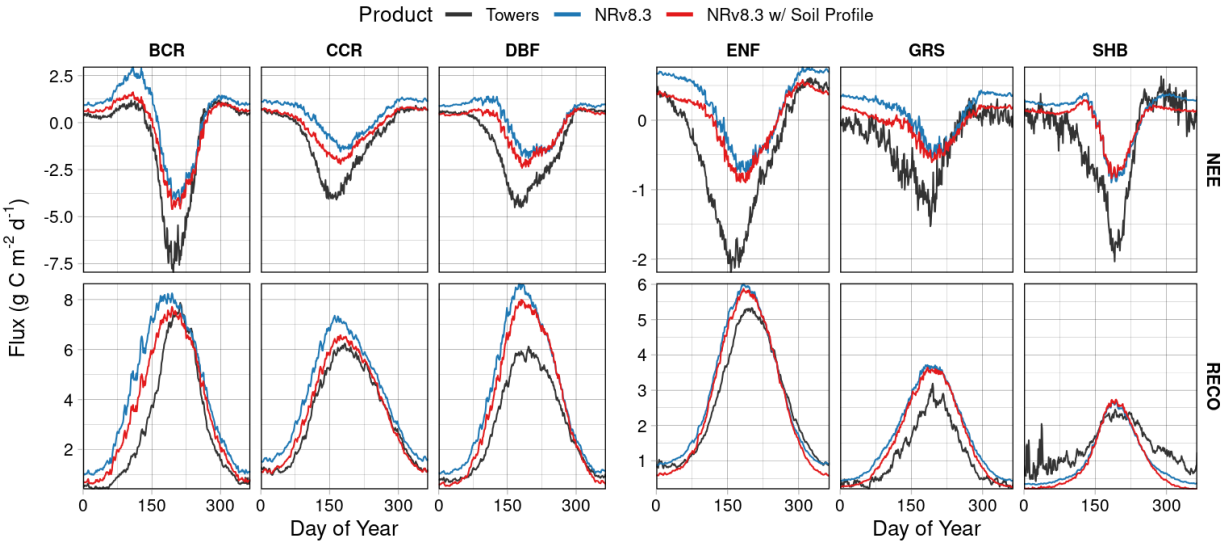


Figure S5: NEE and RECO seasonal cycles at each EC flux tower site in each PFT group, as modeled in the NRv8.3 + Soil Profile experiment.

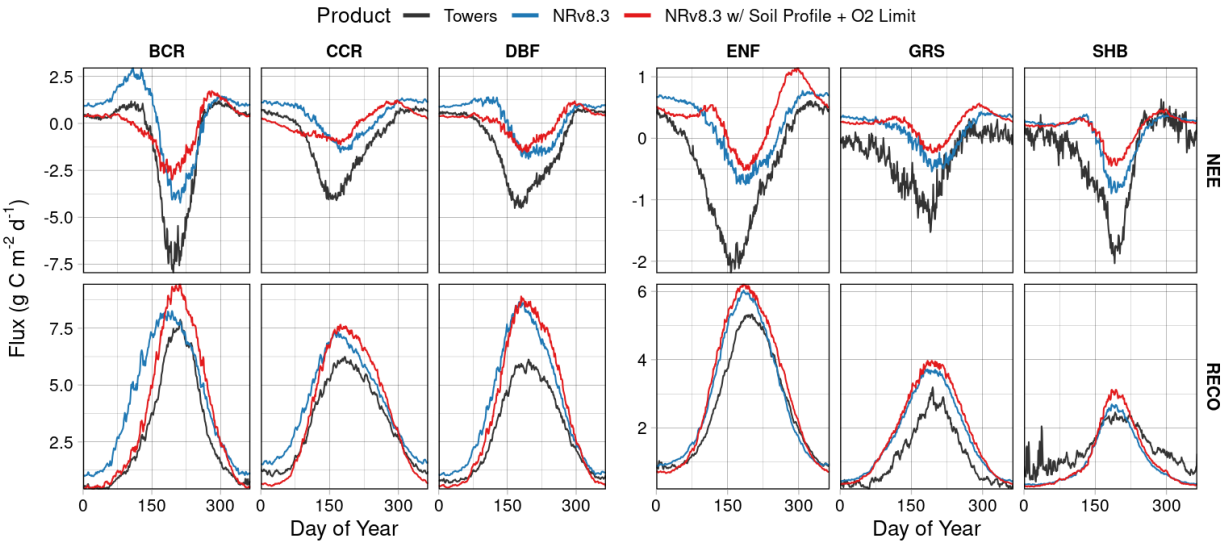


Figure S6: NEE and RECO seasonal cycles at each EC flux tower site in each PFT group, as modeled in the NRv8.3 + Soil Profile + O2 Limit experiment.

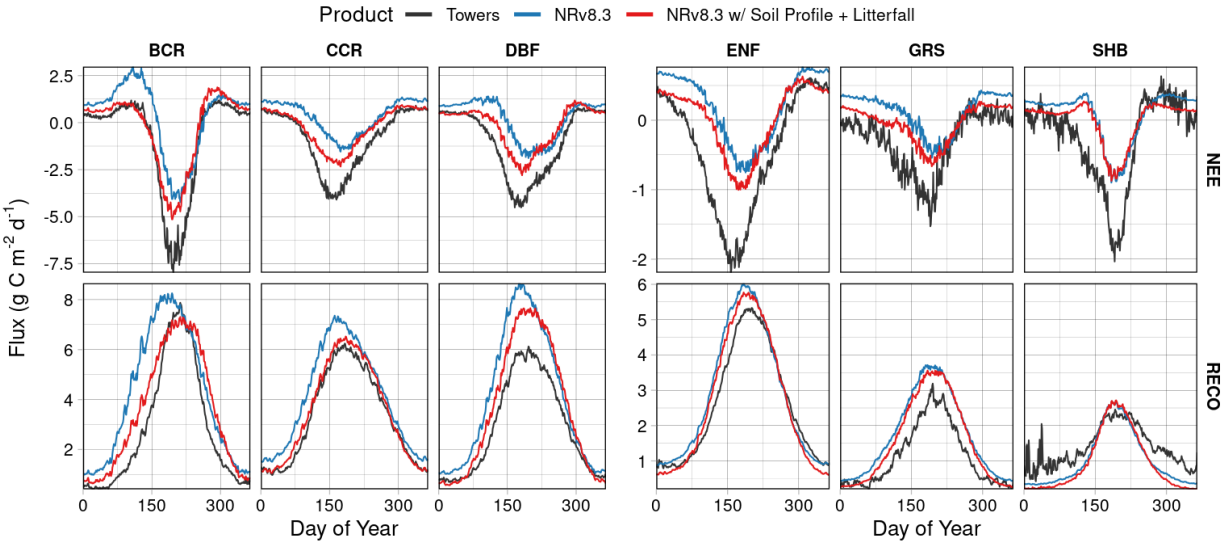


Figure S7: NEE and RECO seasonal cycles at each EC flux tower site in each PFT group, as modeled in the NRv8.3 + Soil Profile + Litterfall experiment.

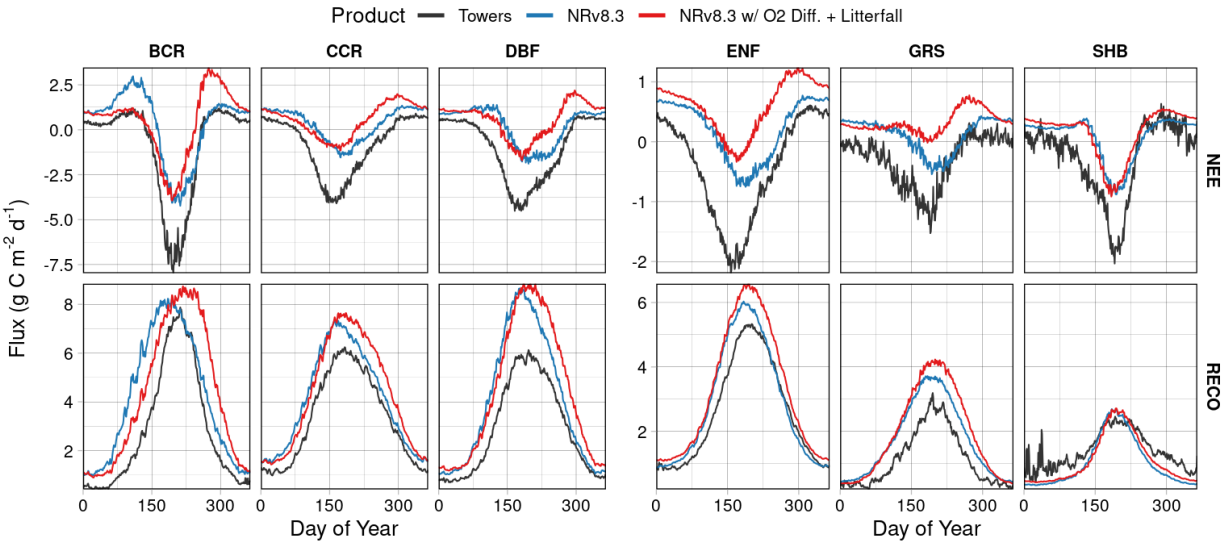


Figure S8: NEE and RECO seasonal cycles at each EC flux tower site in each PFT group, as modeled in the NRv8.3 + O2 Limit + Litterfall experiment.

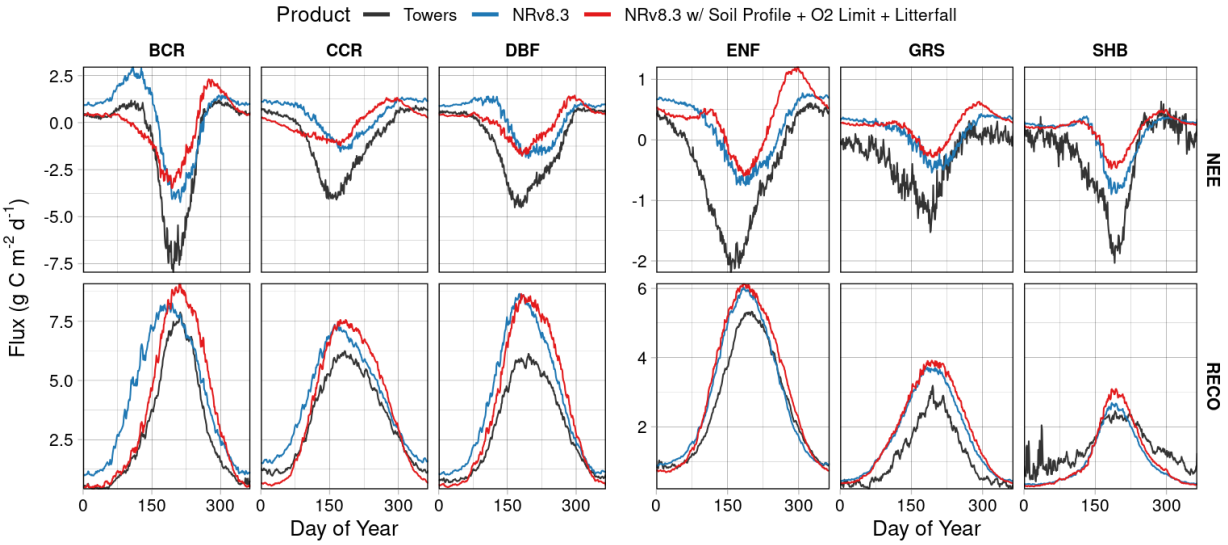


Figure S9: NEE and RECO seasonal cycles at each EC flux tower site in each PFT group, as modeled in the NRv8.3 + Soil Profile + O2 Limit + Litterfall experiment.

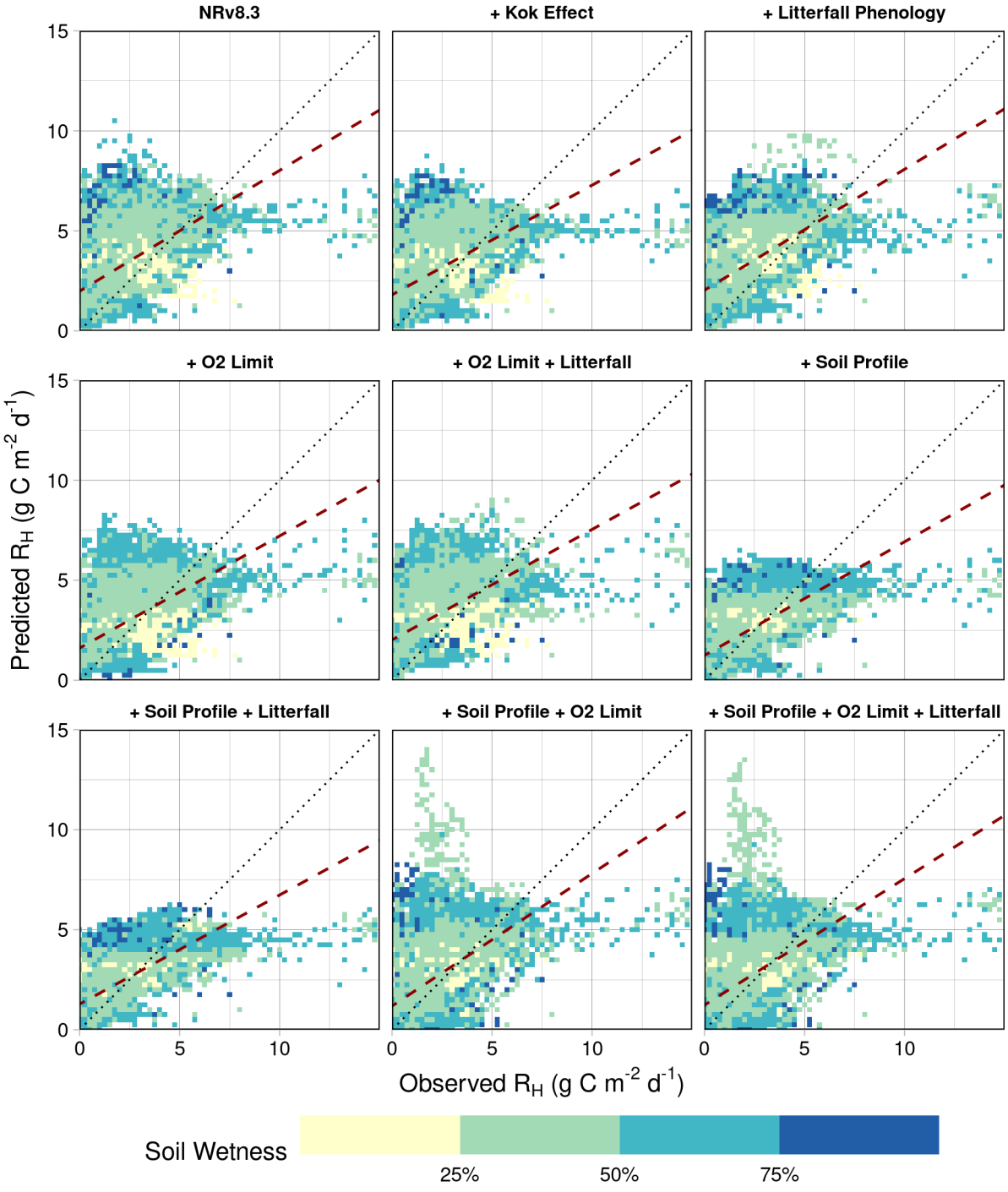


Figure S10: Predicted (modeled) RECO versus observed RECO at COSORE sites for each experiment, for all COSORE sites within an eddy covariance tower footprint or with independent driver data. Soil wetness and $R_H$ are averaged within bins of 0.25 $g\,C\,m^{-2}\,d^{-1}$. Dotted line is the 1:1 line; red dashed line is the line of best fit.

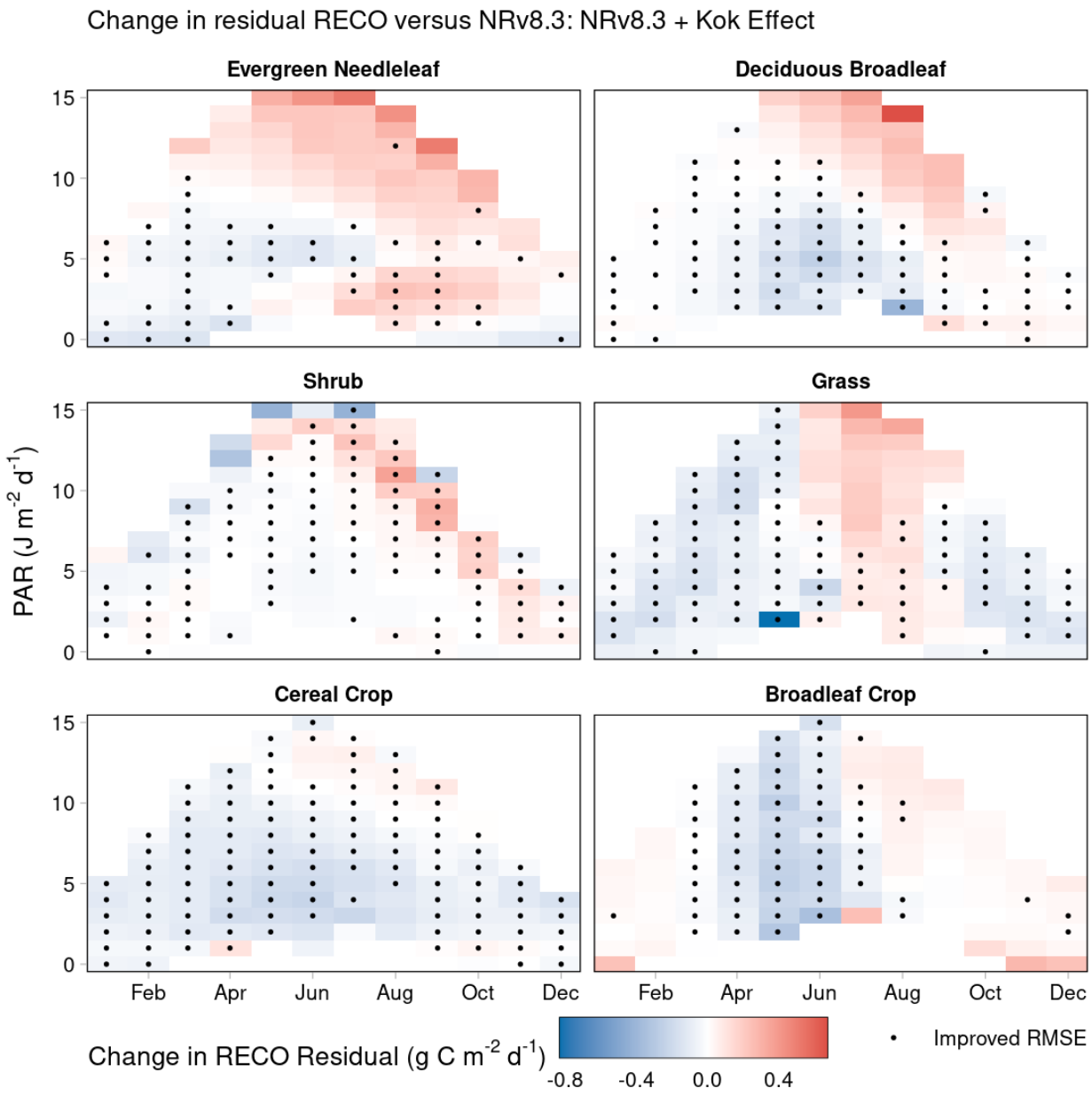


Figure S11: Change in modeled RECO residuals between NRv8.3 and the NRv8.3 + Kok Effect experiment (NRv8.3 minus experiment) for each PFT; shown as mean change in residual for each bin of PAR values by month. A black dot indicates that the change in RECO residual represents an improvement; i.e., a decrease in a high-biased RECO residual or an increase in a low-biased RECO residual.

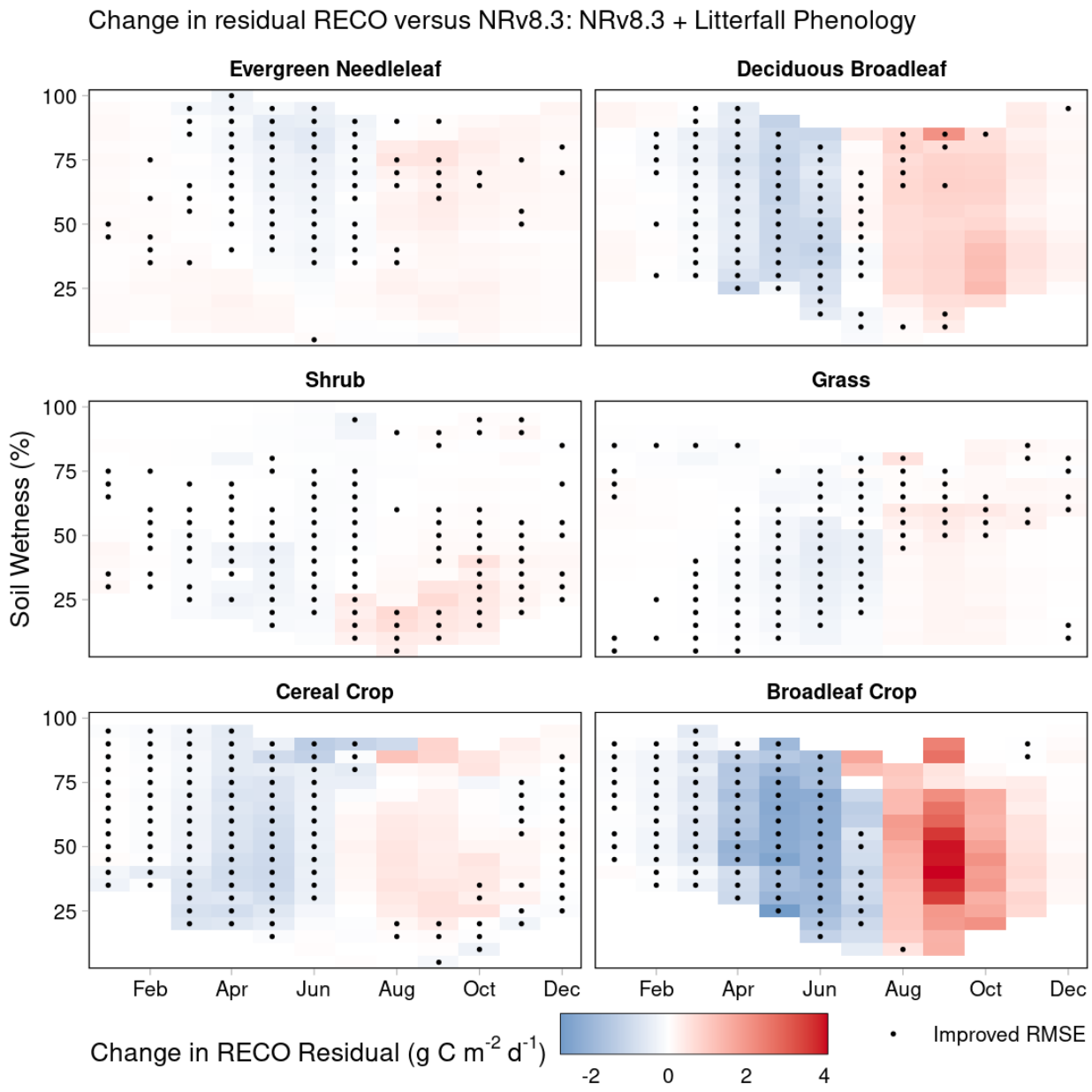


Figure S12: Change in modeled RECO residuals between NRv8.3 and the NRv8.3 + Litterfall Phenology experiment (NRv8.3 minus experiment) for each PFT; shown as mean change in residual for each bin of soil moisture values by month. A black dot indicates that the change in RECO residual represents an improvement; i.e., a decrease in a high-biased RECO residual or an increase in a low-biased RECO residual.

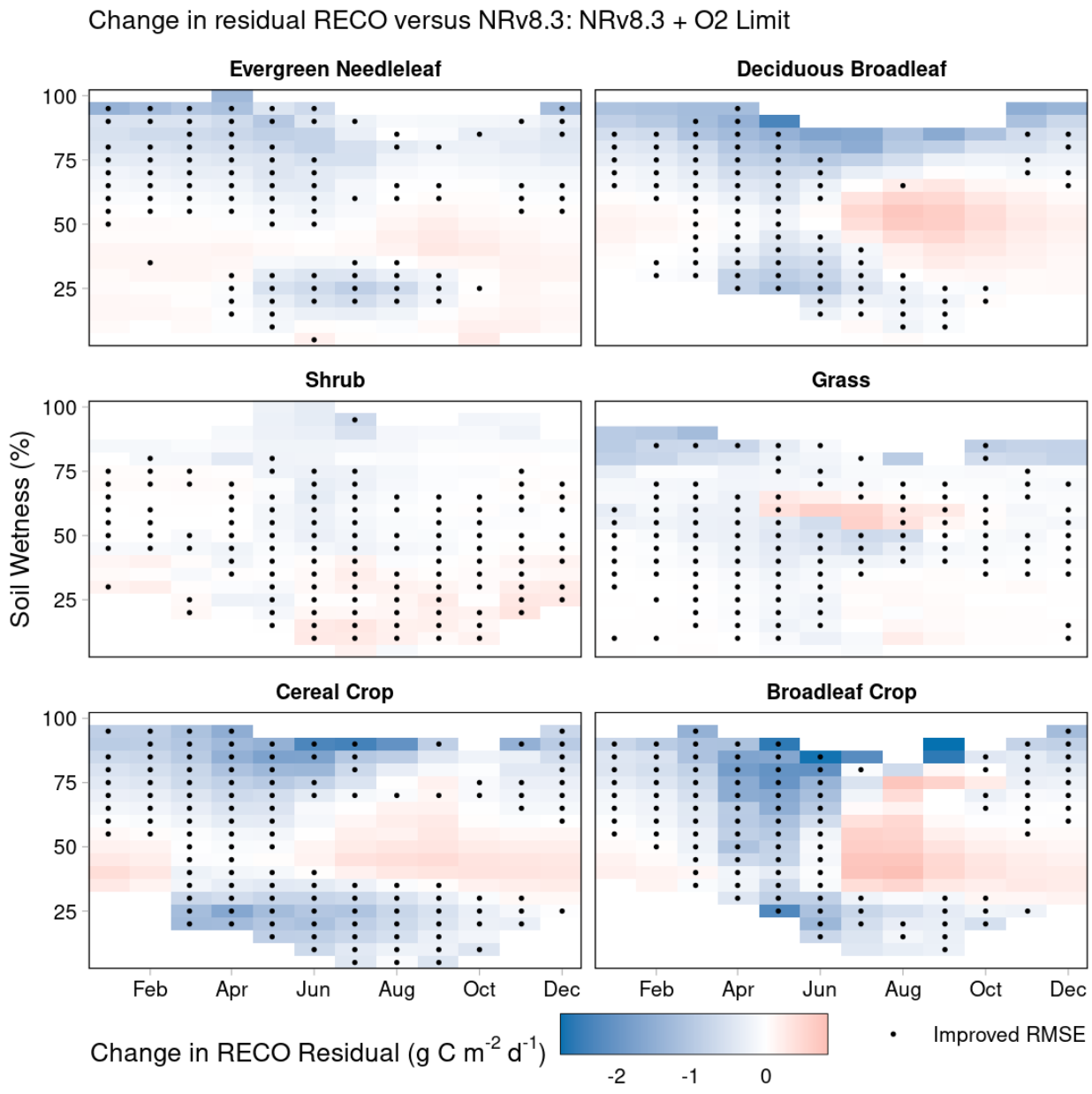


Figure S13: Change in modeled RECO residuals between NRv8.3 and the NRv8.3 + O2 Limit experiment (NRv8.3 minus experiment) for each PFT; shown as mean change in residual for each bin of soil moisture values by month. A black dot indicates that the change in RECO residual represents an improvement; i.e., a decrease in a high-biased RECO residual or an increase in a low-biased RECO residual.

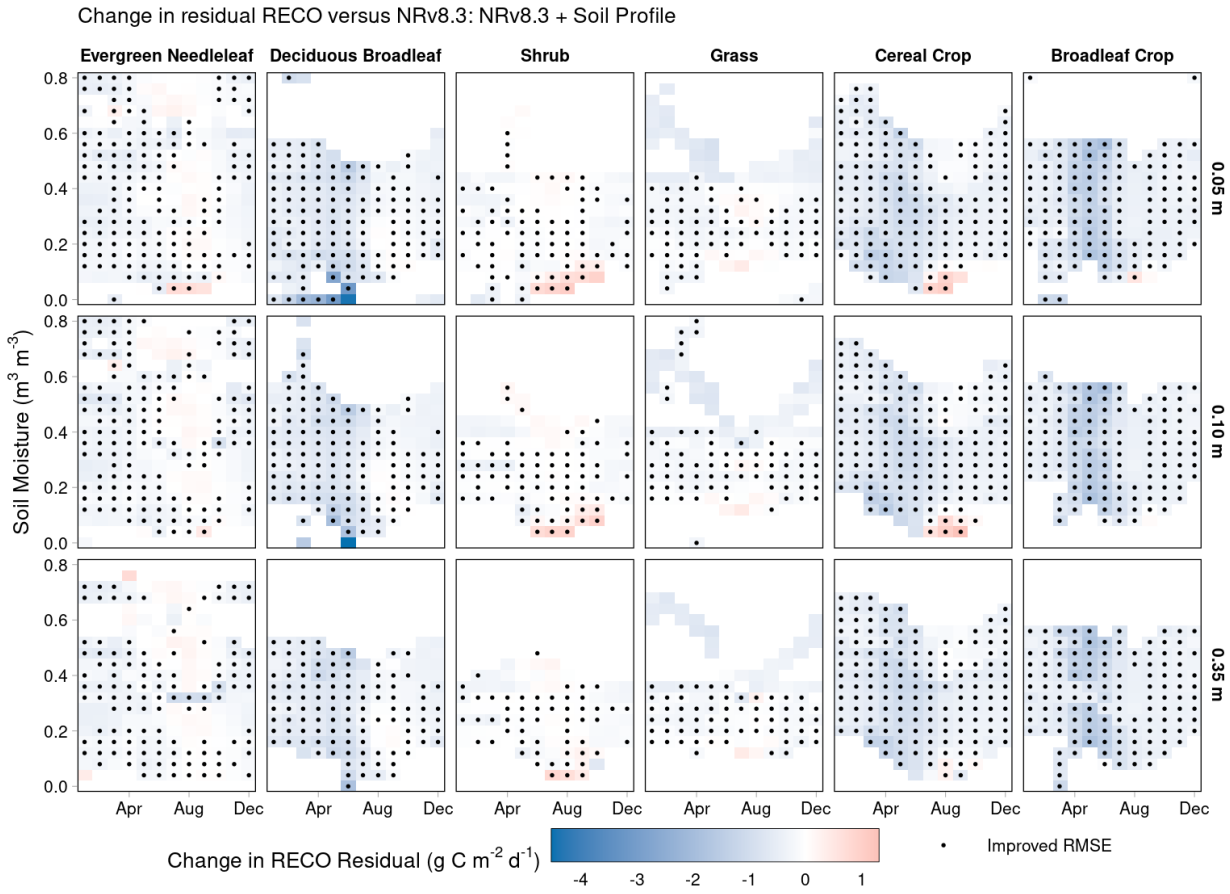


Figure S14: Change in modeled RECO residuals between NRv8.3 and the NRv8.3 + Soil Profile (NRv8.3 minus experiment) for each PFT and each soil layer; shown as mean change in residual for each bin of soil moisture values by month. A black dot indicates that the change in RECO residual represents an improvement; i.e., a decrease in a high-biased RECO residual or an increase in a low-biased RECO residual.

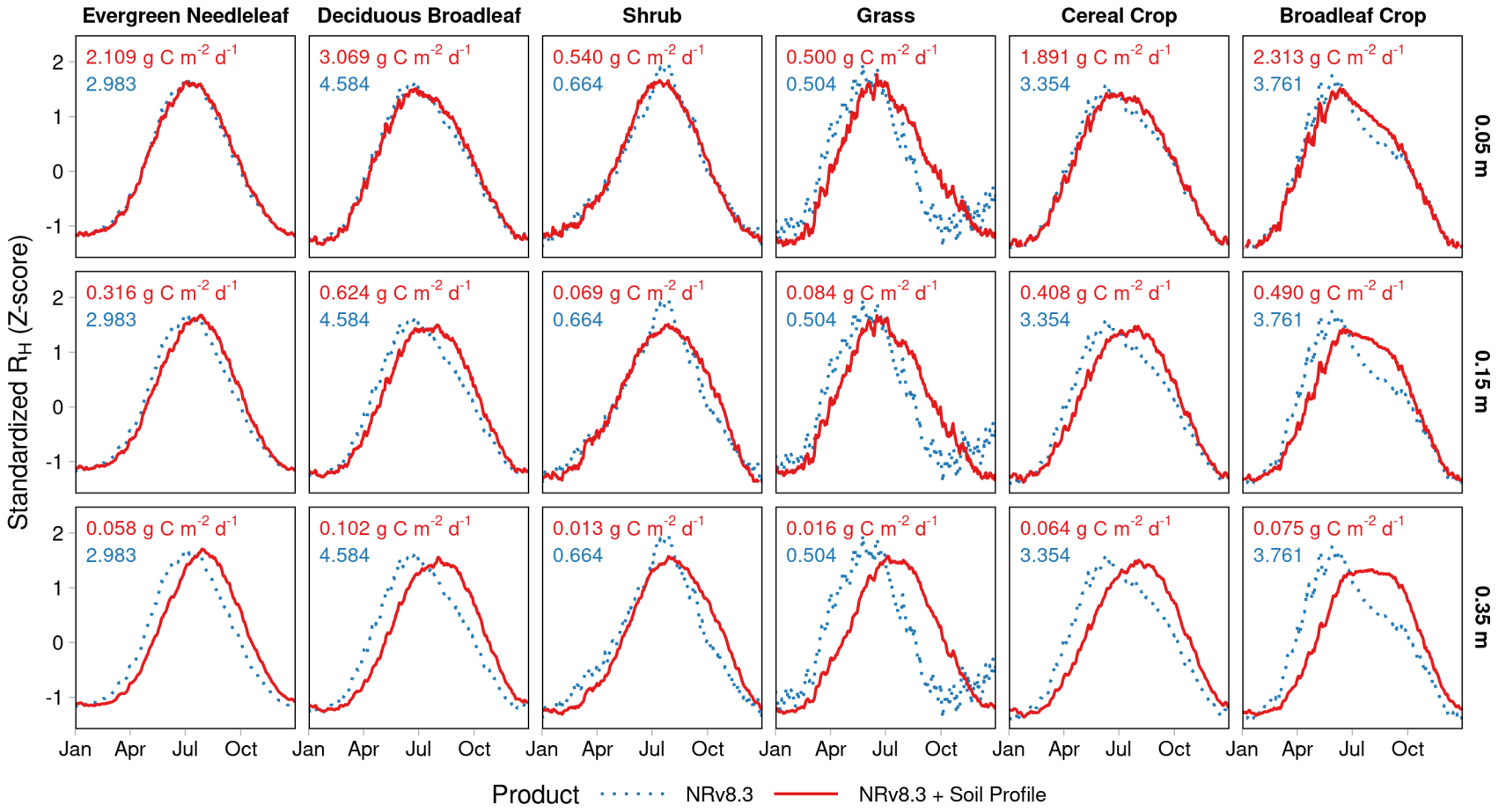


Figure S15: For each PFT, the normalized, mean seasonal cycle of $R_H$ for NRv8.3 and mean seasonal cycle of $R_H$ by depth for the NRv8.3 + Soil Profile experiment. The seasonal amplitude, in carbon units, for both NRv8.3 (blue, dotted line) and NRv8.3 + Soil Profile (red, solid line) are shown in the upper-left of each subplot. Note that the NRv8.3 results are not vertically stratified and therefore do not change across the rows, i.e., they are shown for reference in each soil layer but do not correspond to any single soil layer.

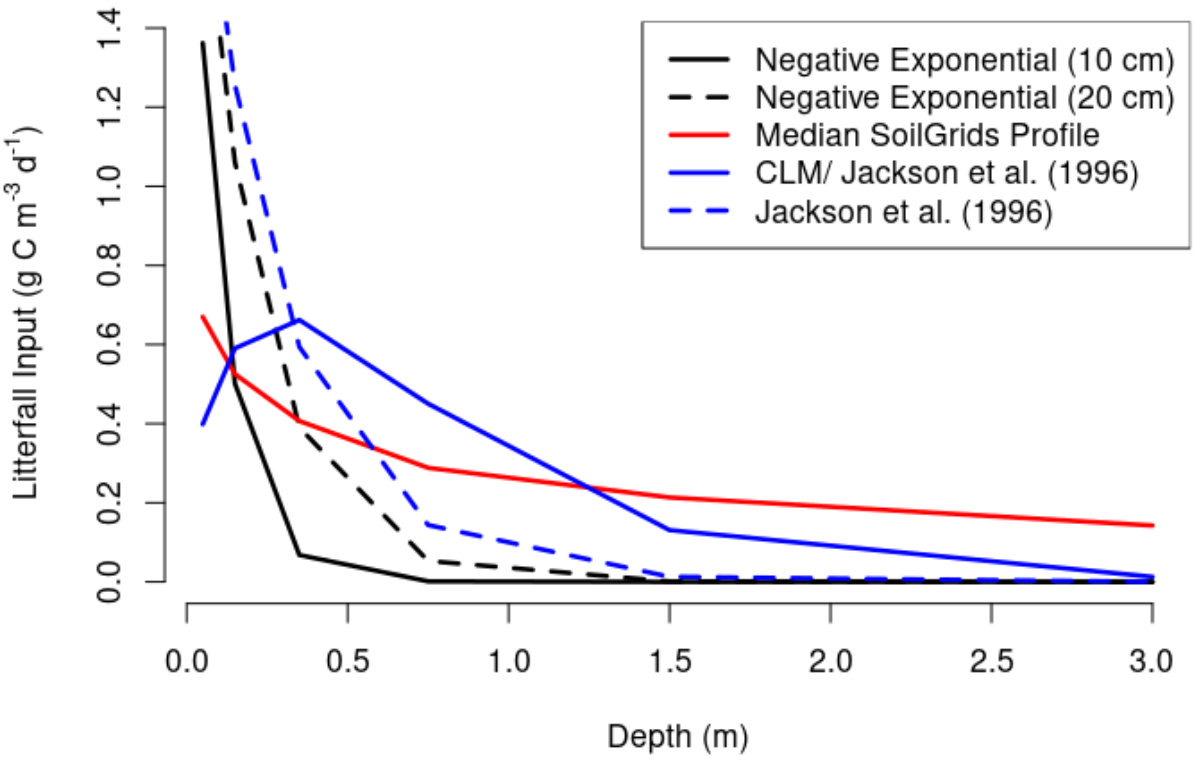


Figure S16: Litterfall input distribution functions, based on the NRv8.3 average daily litterfall (fraction of annual NPP sum). The median SoilGrids profile is from the global SoilGrids 250m product. The CLM/ Jackson et al. (1996) function is described in Lawrence et al. [2018], Equation 2.11.1.

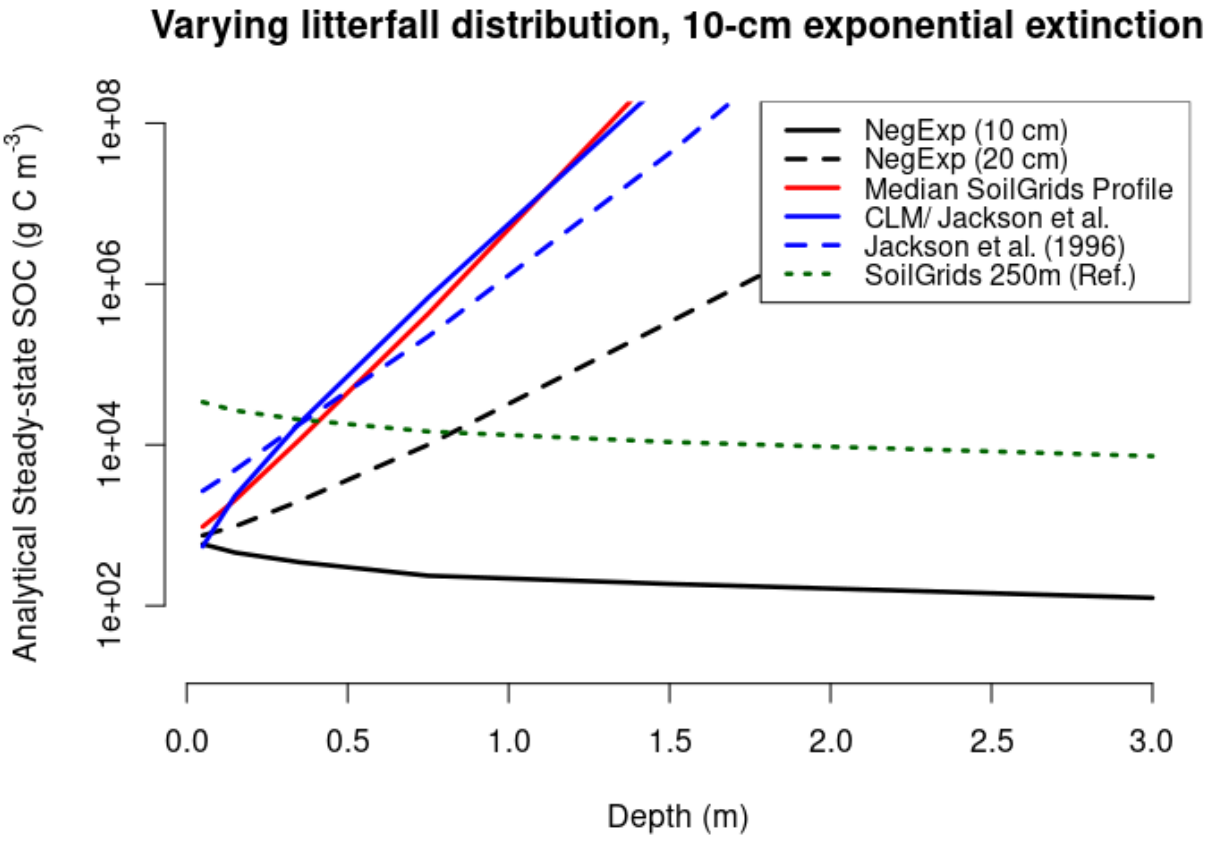


Figure S17: The analytical steady-state soil organic carbon (SOC) distribution, by depth, based on different litterfall input distribution functions and using a negative-exponential extinction function for heterotrophic respiration. The dotted, green line shows the reference SoilGrids 250m SOC profile.

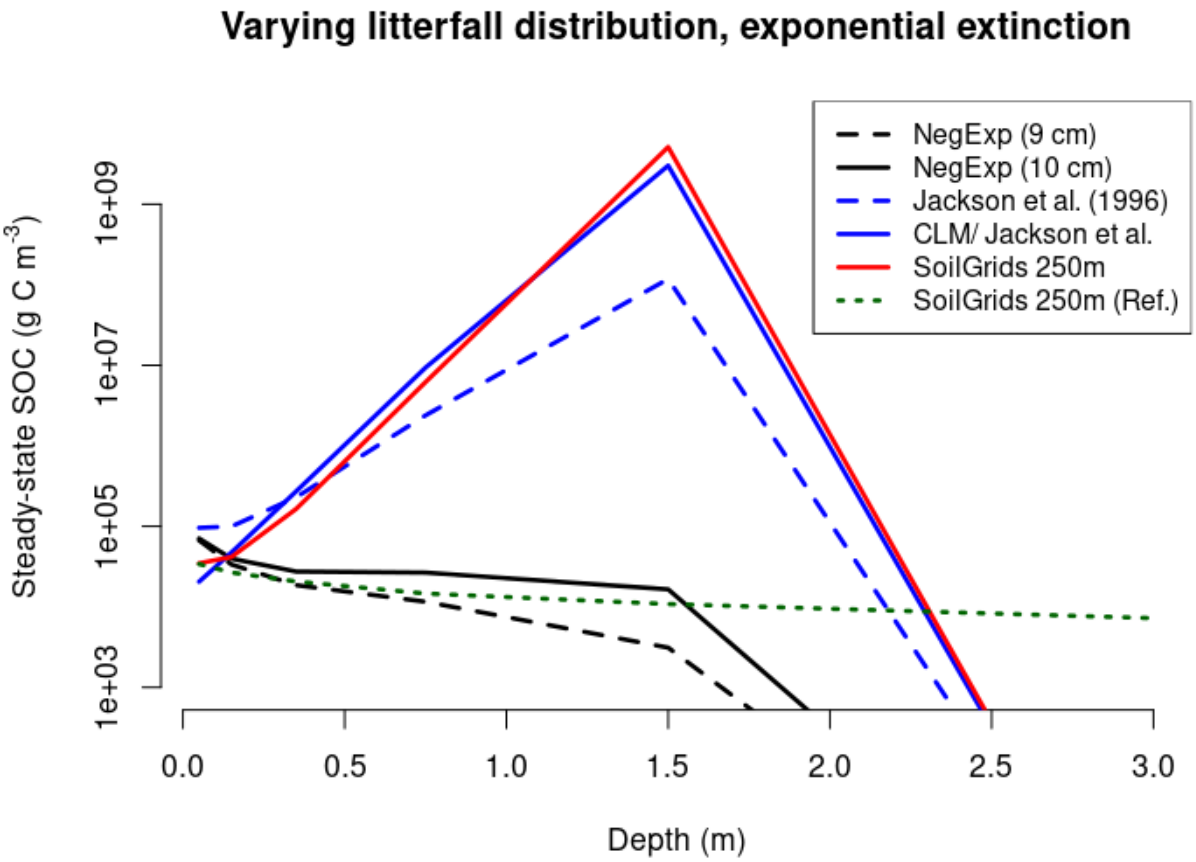


Figure S18: The numerical (final) steady-state soil organic carbon (SOC) distribution, by depth, based on different litterfall input distribution functions and using a negative-exponential extinction function for heterotrophic respiration. The dotted, green line shows the reference SoilGrids 250m SOC profile.

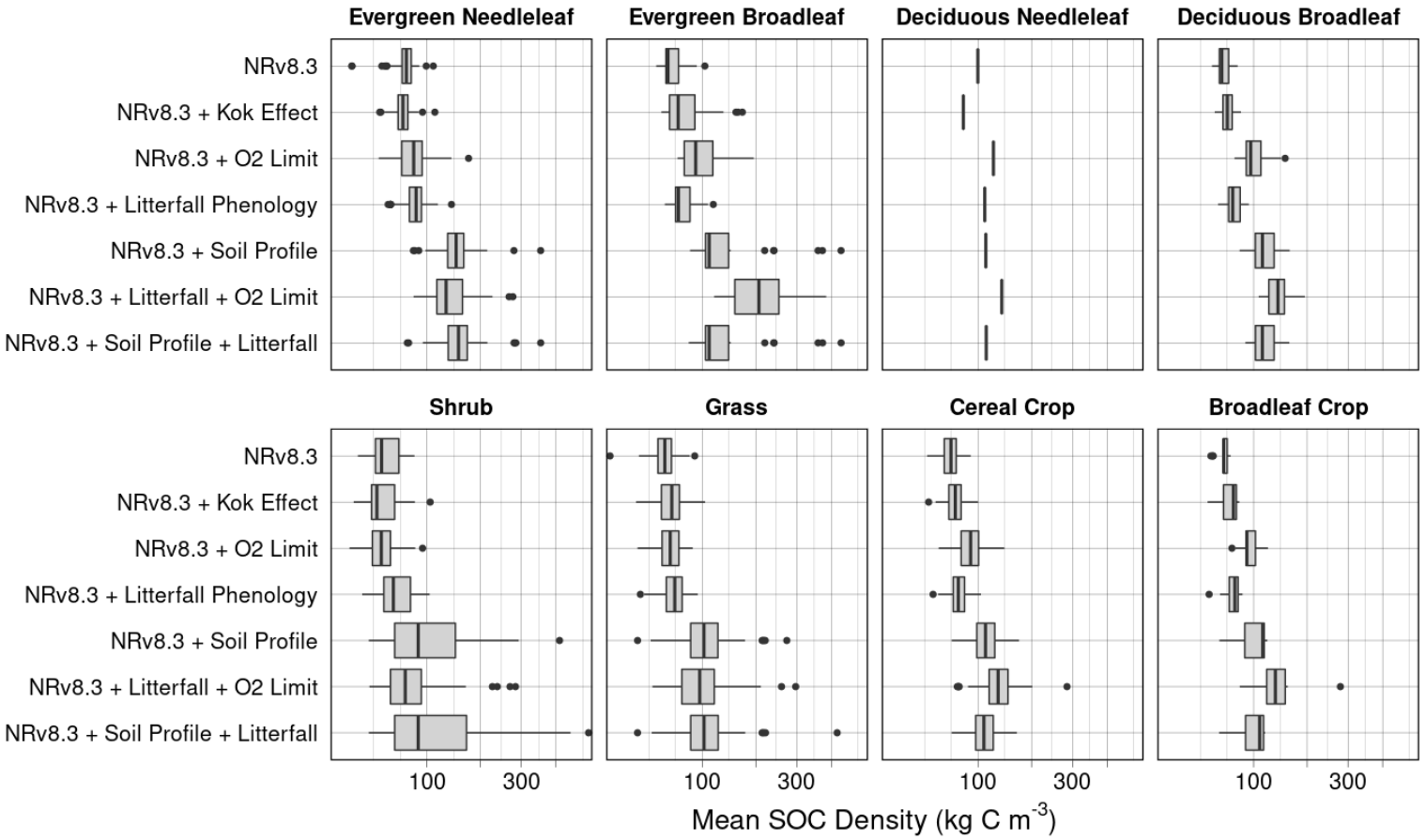


Figure S19: Total soil organic carbon (SOC) content distribution for each experiment, across all sites and all dates.

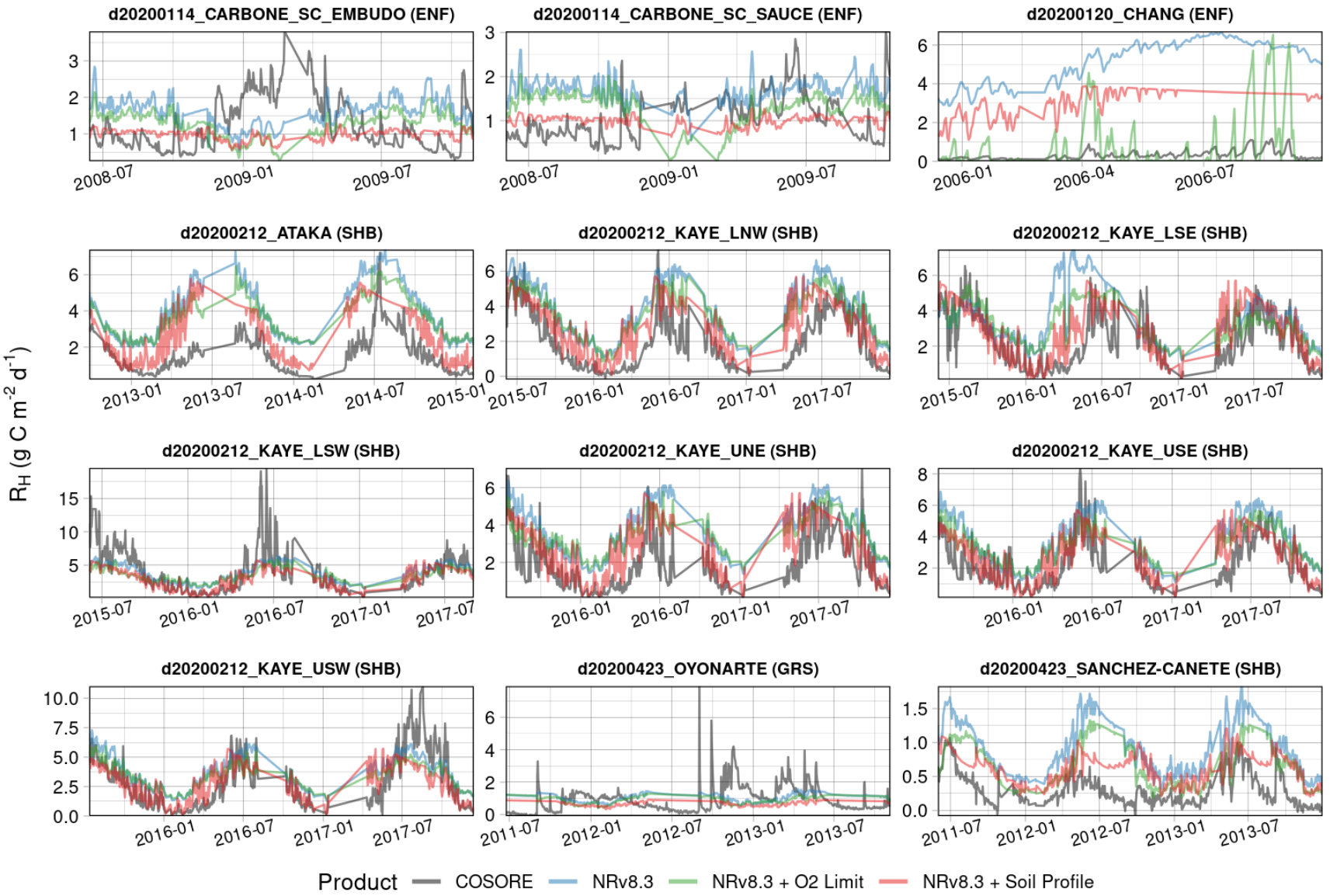


Figure S20: Observed (COSORE) or modeled $R_H$ flux for select experiments, showing only those date ranges wherein COSORE data are available. Of the single-factor experiments, NRv8.3 + Litterfall Phenology is not shown because its dynamics are very similar to NRv8.3.

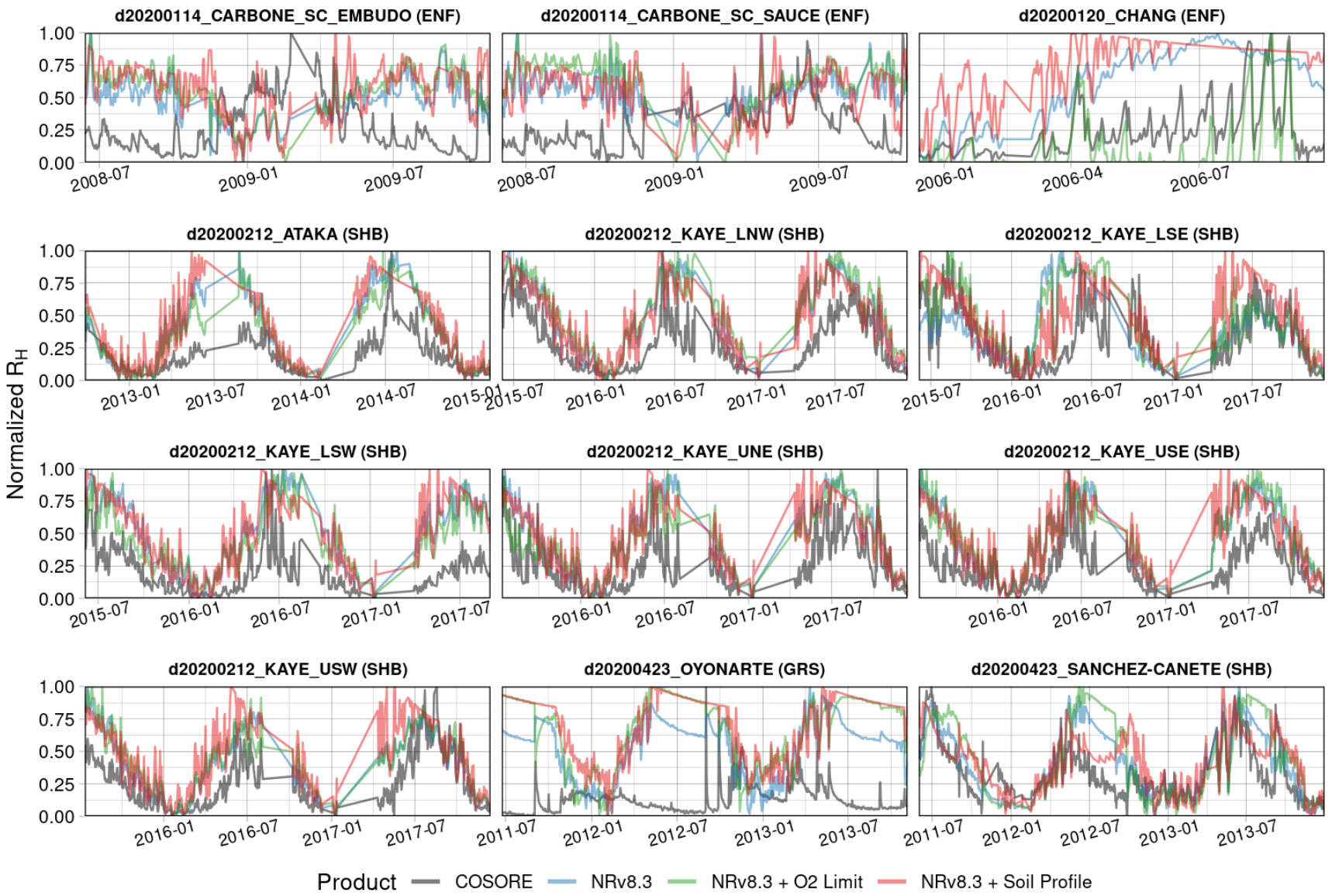


Figure S21: Observed (COSORE) or modeled $R_H$ flux, normalized by each site and product's range in values, for select experiments, showing only those date ranges wherein COSORE data are available. Of the single-factor experiments, NRv8.3 + Litterfall Phenology is not shown because its dynamics are very similar to NRv8.3.

# References


R. G. Allen, L. S. Pereira, D. Raes, and M. Smith. Crop evapotranspiration - Guidelines for computing crop water requirements. Technical report, FAO - Food and Agriculture Organization of the United Nations, Rome, Italy, 1998.

M. A. Arain. AmeriFlux CA-TP3 Ontario - Turkey Point 1974 Plantation White Pine, 2018.

M. Ataka, Y. Kominami, K. Yoshimura, T. Miyama, M. Jomura, and M. Tani. In Situ CO2 Efflux from Leaf Litter Layer Showed Large Temporal Variation Induced by Rapid Wetting and Drying Cycle. *PLoS ONE*, 9(10):e108404, oct 2014. ISSN 1932-6203. doi: 10.1371/journal.pone.0108404. URL https://dx.plos.org/10.1371/journal.pone.0108404.

D. Baldocchi, J. Tang, and L. Xu. How switches and lags in biophysical regulators affect spatial-temporal variation of soil respiration in an oak-grass savanna. *Journal of Geophysical Research: Biogeosciences*, 111(G2):n/a–n/a, jun 2006. ISSN 01480227. doi: 10.1029/2005JG000063. URL http://doi.wiley.com/10.1029/2005JG000063.

V. Balland, J. A. P. Pollacco, and P. A. Arp. Modeling soil hydraulic properties for a wide range of soil conditions. *Ecological Modelling*, 219(3-4):300–316, dec 2008. ISSN 03043800. doi: 10.1016/j.ecolmodel.2008.07.009. URL https://linkinghub.elsevier.com/retrieve/pii/S0304380008003505.

M. S. Carbone, C. J. Still, A. R. Ambrose, T. E. Dawson, A. P. Williams, C. M. Boot, S. M. Schaeffer, and J. P. Schimel. Seasonal and episodic moisture controls on plant and microbial contributions to soil respiration. *Oecologia*, 167(1):265–278, sep 2011. ISSN 0029-8549. doi: 10.1007/s00442-011-1975-3. URL http://link.springer.com/10.1007/s00442-011-1975-3.

M. S. Carbone, A. Park Williams, A. R. Ambrose, C. M. Boot, E. S. Bradley, T. E. Dawson, S. M. Schaeffer, J. P. Schimel, and C. J. Still. Cloud shading and fog drip influence the metabolism of a coastal pine ecosystem. *Global Change Biology*, 19(2):484–497, feb 2013. ISSN 13541013. doi: 10.1111/gcb.12054. URL https://onlinelibrary.wiley.com/doi/10.1111/gcb.12054.

S.-C. Chang, K.-H. Tseng, Y.-J. Hsia, C.-P. Wang, and J.-T. Wu. Soil respiration in a subtropical montane cloud forest in Taiwan. *Agricultural and Forest Meteorology*, 148 (5):788–798, may 2008. ISSN 01681923. doi: 10.1016/j.agrformet.2008.01.003. URL https://linkinghub.elsevier.com/retrieve/pii/S0168192308000026.

R. B. Clapp and G. M. Hornberger. Empirical equations for some soil hydraulic properties. *Water Resources Research*, 14(4):601–604, 1978. ISSN 19447973. doi: 10.1029/WR014i004p00601.

B. J. Cosby, G. M. Hornberger, R. B. Clapp, and T. R. Ginn. A statistical exploration of the relationships of soil moisture characteristics to the physical properties of soils. *Water Resources Research*, 20(6):682–690, 1984. ISSN 19447973. doi: 10.1029/WR020i006p00682.

P. S. Curtis, C. S. Vogel, C. M. Gough, H. P. Schmid, H.-B. Su, and B. D. Bovard. Respiratory carbon losses and the carbon-use efficiency of a northern hardwood forest, 1999–2003. *New Phytologist*, 167(2):437–456, aug 2005. ISSN 0028-646X. doi: 10.1111/j.1469-8137.2005.01438.x. URL https://onlinelibrary.wiley.com/doi/10.1111/j.1469-8137.2005.01438.x.

M. Decker and X. Zeng. An empirical formulation of soil ice fraction based on in situ observations. *Geophysical Research Letters*, 33(5):2–5, 2006. ISSN 00948276. doi: 10.1029/2005GL024914.

M. Detto, G. Bohrer, J. Nietz, K. Maurer, C. Vogel, C. Gough, and P. Curtis. Multivariate Conditional Granger Causality Analysis for Lagged Response of Soil Respiration in a Temperate Forest. *Entropy*, 15(12):4266–4284, oct 2013. ISSN 1099-4300. doi: 10.3390/e15104266. URL http://www.mdpi.com/1099-4300/15/10/4266.

D. Gaumont-Guay, T. A. Black, A. G. Barr, T. J. Griffis, R. S. Jassal, P. Krishnan, N. Grant, and Z. Nesic. Eight years of forest-floor CO2 exchange in a boreal black spruce forest: Spatial integration and long-term temporal trends. *Agricultural and Forest Meteorology*, 184:25–35, jan 2014. ISSN 01681923. doi: 10.1016/j.agrformet.2013.08.010. URL https://linkinghub.elsevier.com/retrieve/pii/S0168192313002177.

R. B. Jackson, J. Canadell, J. R. Ehleringer, H. A. Mooney, O. E. Sala, and E. D. Schulze. A global analysis of root distributions for terrestrial biomes. *Oecologia*, 108:389–411, 1996.

J. Järveoja, M. B. Nilsson, M. Gažovič, P. M. Crill, and M. Peichl. Partitioning of the net CO2 exchange using an automated chamber system reveals plant phenology as key control of production and respiration fluxes in a boreal peatland. *Global Change Biology*, 24(8):3436–3451, 2018. ISSN 13652486. doi: 10.1111/gcb.14292.

R. S. Jassal, T. A. Black, M. D. Novak, D. Gaumont-Guay, and Z. Nesic. Effect of soil water stress on soil respiration and its temperature sensitivity in an 18-year-old temperate Douglas-fir stand. *Global Change Biology*, 14(6):1305–1318, jun 2008. ISSN 13541013. doi: 10.1111/j.1365-2486.2008.01573.x. URL https://onlinelibrary.wiley.com/doi/10.1111/j.1365-2486.2008.01573.x.

D. Lawrence, R. Fisher, C. Koven, K. Oleson, S. Swenson, M. Vertenstein, B. Andre, G. Bonan, B. Ghimire, L. van Kampenhout, D. Kennedy, E. Kluzek, P. L. Ryan Knox, F. Li, H. Li, D. Lombardozzi, Y. Lu, J. Perket, W. Riley, WilliamSacks, M. Shi, W. Wieder, and C. Xu. Technical Description of version 5.0 of the Community Land Model (CLM). Technical report, University Corporation for Atmospheric Research (UCAR), 2018. URL https://escomp.github.io/ctsm-docs/versions/release-clm5.0/html/tech{_}note/index.html.

D. M. Lawrence, R. A. Fisher, C. D. Koven, K. W. Oleson, S. C. Swenson, G. B. Bonan, N. Collier, B. Ghimire, L. Kampenhout, D. Kennedy, E. Kluzek, P. J. Lawrence, F. Li, H. Li, D. Lombardozzi, W. J. Riley, W. J. Sacks, M. Shi, M. Vertenstein, W. R. Wieder, C. Xu, A. A. Ali, A. M. Badger, G. Bisht, M. Broeke, M. A. Brunke, S. P. Burns, J. Buzan, M. Clark, A. Craig, K. Dahlin, B. Drewniak, J. B. Fisher, M. Flanner, A. M. Fox, P. Gentine, F. Hoffman, G. Keppel-Aleks, R. Knox, S. Kumar, J. Lenaerts, L. R. Leung,

W. H. Lipscomb, Y. Lu, A. Pandey, J. D. Pelletier, J. Perket, J. T. Randerson, D. M. Ricciuto, B. M. Sanderson, A. Slater, Z. M. Subin, J. Tang, R. Q. Thomas, M. Val Martin, X. Zeng, and ... The Community Land Model version 5: Description of new features, benchmarking, and impact of forcing uncertainty. *Journal of Advances in Modeling Earth Systems*, 11(12):4245–4287, dec 2019. ISSN 1942-2466. doi: 10.1029/2018MS001583. URL https://onlinelibrary.wiley.com/doi/abs/10.1029/2018MS001583.

Q. Mu, M. Zhao, and S. W. Running. Improvements to a MODIS global terrestrial evapotranspiration algorithm. *Remote Sensing of Environment*, 115(8):1781–1800, 2011. ISSN 00344257. doi: 10.1016/j.rse.2011.02.019. URL http://dx.doi.org/10.1016/j.rse.2011.02.019.

A. Noormets, M. J. Gavazzi, S. G. Mcnulty, J.-C. Domec, G. Sun, J. S. King, and J. Chen. Response of carbon fluxes to drought in a coastal plain loblolly pine forest. *Global Change Biology*, 16(1):272–287, jan 2010. ISSN 13541013. doi: 10.1111/j.1365-2486.2009.01928.x. URL https://onlinelibrary.wiley.com/doi/10.1111/j.1365-2486.2009.01928.x.

K. Oleson, D. M. Lawrence, G. B. Bonan, B. Drewniak, M. Huang, C. D. Koven, S. Levis, F. Li, W. J. Riley, Z. M. Subin, S. Swenson, P. E. Thornton, A. Bozbiyik, R. Fisher, C. L. Heald, E. Kluzek, J.-F. Lamarque, P. J. Lawrence, L. R. Leung, W. Lipscomb, S. P. Muszala, D. M. Ricciuto, W. J. Sacks, Y. Sun, J. Tang, and Z.-L. Yang. Technical description of version 4.5 of the Community Land Model (CLM). Technical report, 2013.

E. P. Sánchez-Cañete, C. Oyonarte, P. Serrano-Ortiz, J. Curiel Yuste, O. Pérez-Priego, F. Domingo, and A. S. Kowalski. Winds induce CO2 exchange with the atmosphere and vadose zone transport in a karstic ecosystem. *Journal of Geophysical Research: Biogeosciences*, 121(8):2049–2063, aug 2016. ISSN 21698953. doi: 10.1002/2016JG003500. URL http://doi.wiley.com/10.1002/2016JG003500.

UCAR. The Community Terrestrial Systems Model, 2020. URL https://github.com/ESCOMP/CTSM.

M. Ueyama, K. Yoshikawa, and K. Takagi. A cool-temperate young larch plantation as a net methane source - A 4-year continuous hyperbolic relaxed eddy accumulation and chamber measurements. *Atmospheric Environment*, 184:110–120, jul 2018. ISSN 13522310. doi: 10.1016/j.atmosenv.2018.04.025. URL https://linkinghub.elsevier.com/retrieve/pii/S1352231018302565.

R. Vargas, E. Sánchez-Cañete P, P. Serrano-Ortiz, J. Curiel Yuste, F. Domingo, A. López-Ballesteros, and C. Oyonarte. Hot-Moments of Soil CO2 Efflux in a Water-Limited Grassland. *Soil Systems*, 2(3):47, aug 2018. ISSN 2571-8789. doi: 10.3390/soilsystems2030047. URL http://www.mdpi.com/2571-8789/2/3/47.

A. Verhoef and G. Egea. Modeling plant transpiration under limited soil water: Comparison of different plant and soil hydraulic parameterizations and preliminary implications for their use in land surface models. *Agricultural and Forest Meteorology*, 191:22–32, 2014. ISSN 01681923. doi: 10.1016/j.agrformet.2014.02.009. URL http://dx.doi.org/10.1016/j.agrformet.2014.02.009.

Q. Zhang, R. P. Phillips, S. Manzoni, R. L. Scott, A. C. Oishi, A. Finzi, E. Daly, R. Vargas, and K. A. Novick. Changes in photosynthesis and soil moisture drive the seasonal soil respiration-temperature hysteresis relationship. *Agricultural and Forest Meteorology*, 259: 184–195, sep 2018. ISSN 01681923. doi: 10.1016/j.agrformet.2018.05.005. URL https://linkinghub.elsevier.com/retrieve/pii/S0168192318301515.